



Thermal behavior of natural stellerite: high-temperature X-ray powder diffraction and IR spectroscopy study

Ekaterina Kaneva^{1,2} · Roman Shendrik¹

Received: 4 July 2022 / Accepted: 29 August 2022 / Published online: 12 September 2022
© The Author(s), under exclusive licence to The Japan Society for Analytical Chemistry 2022

Abstract

The thermal behavior of stellerite from the Savinskoye deposit (Transbaikalia, Russia), $\text{Ca}_{7.69}\text{Na}_{0.25}\text{K}_{0.06}(\text{Si}_{56.24}\text{Al}_{15.76})\text{O}_{144}\cdot 53.39\text{H}_2\text{O}$, was investigated by in situ high-temperature X-ray powder diffraction (HTXRPD) and ex situ HT infrared (IR) spectroscopic analysis. Four different HTXRPD experimental procedures were used to study the thermal behavior of the powder samples: (1) RT–750 °C, (2) RT–220 °C –RT, (3) 200–350–RT °C, and (4) 350–700 °C. Electron probe microanalysis and single-crystal X-ray diffraction were preliminary used to determine the chemical composition and crystal structure of stellerite. The A → B phase transition ($Fm\bar{3}m \rightarrow Amma$) starts at ~110 °C and is completed at about 140 °C (in situ HTXRPD) and 200 °C (ex situ HTIR) depending on the experimental conditions. It involves a cell volume decrease of 5.8% (Experiment 1). The thermal expansion of stellerite is more pronounced along the *b* and *c* axes, with $\alpha_a : \alpha_b : \alpha_c (\times 10^{-5}) = 2.50 : -25.52 : -6.84$ at 100 °C, $0.44 : -21.75 : -25.64$ at 150 °C after the completion of the phase transition, and $3.06 : -1.86 : -16.94$ at 500 °C. The reverse B → A transition occurs at temperatures below 100 °C during slow cooling (Experiment 2), however, it does not occur upon rapid cooling (Experiment 3). The B → D phase transition above 300 °C is not observed (Experiment 4). The temperature barrier of phase transition in the ex situ HTIR spectroscopy experiment is shifted towards high temperatures. The heating above 200 °C leads to an increase of 3430 cm^{-1} and a decrease of 3600 and 3260 cm^{-1} bands, which correspond to the stretching vibration of H_2O . The heating above 400 °C causes complete dehydration of the stellerite.

Keywords Stellerite · Zeolite · Thermal behavior · Rehydration · HTXRPD · IR spectroscopy

Introduction

Zeolite minerals have clearly demonstrated their potential in industrial applications. Most of the studies on stilbite subgroup representatives were aimed at investigating the mineralogy, crystal chemistry, and cation and water adsorption properties of the minerals. This subgroup is represented by the barrerite–stilbite–Na–stilbite–Ca–stellerite series. The end members, barrerite and stellerite, are orthorhombic, while the stilbite varieties are monoclinic, but the differences are subtle. In this regard, it is difficult to detect them only using X-ray diffraction, and it is necessary to confirm the chemical composition of the variety.

Stellerite (CNMMN/CNMNC approved formula: $\text{Ca}_4(\text{Si}_{28}\text{Al}_8)\text{O}_{72}\cdot 28\text{H}_2\text{O}$; space group $Fm\bar{3}m$) has the STI framework type (code defined in [1]). A STI-type framework can be described by the connection of the 4^25^4 secondary building units (SBUs) to form chains parallel to the *c* axis (Fig. S1 a,b, submitted as supplementary material). These chains are joined laterally by six oxygens to form layers parallel to the *ac* plane (Fig. S2). Two other bridging oxygens link the layers to each other, forming a three-dimensional net. As a result, two systems of structural channels are formed: a 10-ring channel running parallel to the *a* axis (Fig. S1 c), and an 8-ring channel running along the *c* axis. The eight Ca cations per unit cell, surrounded by water molecules, are located in one set of equivalent extraframework positions almost in the center of the 10-ring channel (Fig. 1 and Fig. S2).

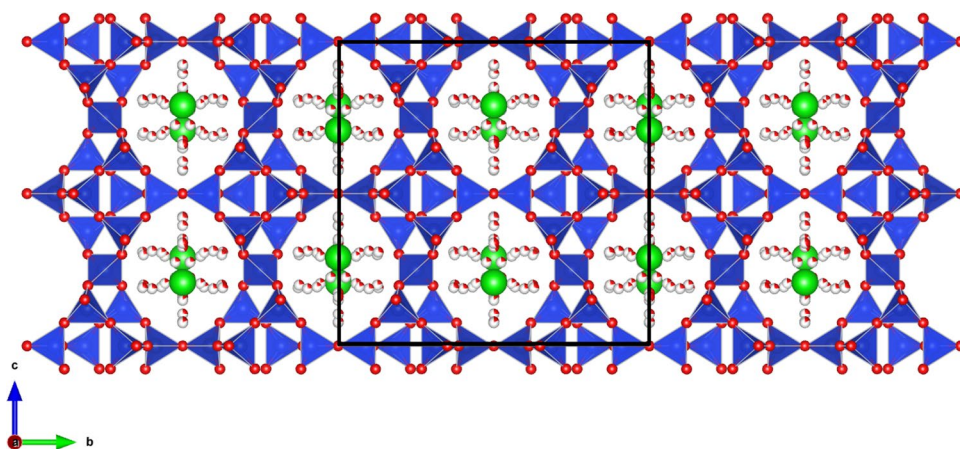
The thermal behavior of the stilbite family compounds has been investigated extensively since the 30 s of the last century (for example [2–6]). However, until the 70 s, the results obtained were contradictory. Nevertheless, it became

✉ Ekaterina Kaneva
kev604@mail.ru

¹ Vinogradov Institute of Geochemistry SB RAS, 1a Favorsky Str, 664033 Irkutsk, Russia

² Sidorov Mineralogical Museum, Irkutsk National Research Technical University, 664074 Irkutsk, Russia

Fig. 1 Crystal structure of studied stellerite projected along [100]. Oxygen atoms are drawn in red. Mixed Si–Al tetrahedra are blue. Ca positions are designated as green spheres. The partially white coloring of the spheres indicates a partially occupied sites. The unit cell is shown



clear that having different chemical compositions and symmetries, barrerite, stilbite, and stellerite are characterized by different thermal behaviors.

Barrerite ($\text{Na}_2(\text{Si}_7\text{Al}_2)\text{O}_{18} \cdot 6\text{H}_2\text{O}$ – CNMMN/CNMNC approved formula) is orthorhombic, having an *Amma* space group [7, 8], while stilbite ($\text{Na}_9(\text{Si}_{27}\text{Al}_9)\text{O}_{72} \cdot 28\text{H}_2\text{O}$ and $\text{NaCa}_4(\text{Si}_{27}\text{Al}_9)\text{O}_{72} \cdot 28\text{H}_2\text{O}$ for Na-stilbite and Ca-stilbite, respectively) is monoclinic *C2/m* (or pseudo-orthorhombic setting *F2/m*) [9–11]. At room temperature, stellerite represents the so-called A-phase (*Fmmm*). With an increase in temperature, structural modifications occur with the formation of a new phase, the B-phase with the *Amma* space group [12–16]. This transformation occurs at a temperature of about 160 °C [16]. According to other later data at temperature > 300 °C the B-phase of stellerite was found to be monoclinic (sp. gr. *A2/m*, [17]). Barrerite transformed into the B-phase (sp. gr. *Amma*) at the temperature of ~ 250 °C [18], while at ~ 175 °C the B-phase (sp. gr. *A2/m*) of stilbite occurs [17, 19]; previously, Cruciani et al. (1997) [11] proposed a space group *Amma* for the B-phase of stilbite). Finally, only for barrierite mineral a D phase (sp. gr. *A2₁ma*) is formed, which has a transition temperature near 400–450 °C [20, 21]. At temperatures above 500–550 °C, all phases transform into an amorphous state.

It should be noted that in the fundamental work of Alberti and Martucci (2005) [22], the study of the thermal behavior of zeolites with STI framework type [1], as far as HEU, BRE, LOS, and EAB, was found to be especially interesting. A dehydration process of these compounds is accompanied by the formation of new phases and structural modifications due to the statistical breaking of framework T–O–T bonds [22]. Arletti et al. (2006) [16] discussed the influence of dehydration kinetics in more detail for the stellerite sample, which was used for a temperature-resolved X-ray powder diffraction experiment using synchrotron radiation. Cametti et al. (2017) [17], Cametti et al. (2019) [23] and Cametti et al. (2019) [24] devoted their studies to the thermal behavior and thermal stability of Na-, Ag- and Cd-exchanged

forms of stellerite, respectively. They used an *in situ* high-temperature (HT) single-crystal X-ray diffraction (SCXRD) method, comparing the results with those obtained for a natural mineral. In addition, the high-pressure behavior of stilbite group minerals was investigated [25–27].

Despite the fact that quite a lot of data devoted to the study of the thermal behavior of stellerite obtained by the single crystal and powder X-ray diffraction have been published, the method of infrared (IR) spectroscopy has practically not been used for these purposes. Several publications contain IR spectra of minerals of the stilbite group (for example, [28, 29]), but they were obtained at room temperature, and the features of the spectral shape changes with increasing temperature were studied only for stilbite [30].

It should be noted that we have already successfully used HT IR spectroscopy to study the crystal-chemical features of some natural silicate compounds (see, for example, [31–34]).

The aims of this work are (1) to study the dehydration dynamics of stellerite by *in situ* high-temperature X-ray powder diffraction (HT XRPD); (2) to characterize the thermal behavior of stellerite by IR spectroscopic *ex situ* experiments; and (3) to compare the results with each other and with previously published data [8, 11, 12].

Material and methods

Geological context and sample description

Stellerite samples were selected from rock fragment from the Savinskoye deposit, which belongs to the Klichinskaya group of deposits, Transbaikalia, Russia. It is located 500 m north of the Klichka village (former Nerchinsk mountain district). The deposit belongs to the vein lead–zinc formation and is confined to the interbedding of terrigenous and carbonate rocks at the boundary of the Nortuyskaya and Klichinskaya formations, intruded by quartz diorites of the Kadain complex, dikes of dolerites and lamprophyres.

The host rocks are hornfelsed and skarned. Approximately 40 ore bodies have been identified, occurring in accordance with the bedding of sedimentary rocks and controlled by faults in the zone of the submeridional Tsagan-Zolotuysky fault [35]. The ore bodies are composed of quartz, carbonates, pyrite, pyrrhotite, galena, sphalerite, arsenopyrite with a minor marcasite, chalcopyrite, tetrahedrite, and bornite. They are split by cracks filled with quartz, calcite, fluorite, zeolites. Sometimes there are cavities with a volume of up to 10 m³ on the walls of which well-faceted crystals of the listed minerals grow [36].

Stellerite is found in cavities (up to 2 × 1.5 × 2 m) in the form of drusoid lamellar outgrowths of yellowish-gray and colorless translucent crystals with associated lamellar calcite crystals up to 8–10 cm in size. Also, closely intergrown crystals of lamellar stellerite in the form of crusts up to 2.5–3 cm thick were found in veins [37].

Chemical analysis

The chemical composition of the stellerite was studied on single crystals embedded in epoxy resin, polished and carbon-coated. A JEOL JXA-8230 electron microprobe (JEOL, Tokyo, Japan) operating at 20 kV accelerating voltage, 10 nA beam current, and a ~ 10 μm spot size in wavelength-dispersive spectroscopic (WDS) mode. The following standards were employed: F-phlogopite (Si, Al, K, Mg), diopside (Ca), albite (Na), Mn-garnet rhodonite (Mn), pyrope (Fe), Sr-glass (Sr), BaSO₄ (Ba). For the conversion from X-ray counts to oxide weight percentages (wt.%), a Phi-Rho-Z (PAP) [38] matrix-correction method was employed as implemented in the JEOL (Tokyo, Japan) suite of the program.

XRD investigation

The crystal structure of the stellerite at room temperature was studied using a Bruker AXS D8 VENTURE automated diffractometer (Bruker, Berlin, Germany) equipped with a Photon 100 detector, and MoK α radiation. The operating conditions were 50 kV and 1 mA; the crystal-to-detector distance was 40 mm. The collection strategy was optimized by the APEX2 (Version 2014.11–0, Bruker AXS Inc.: Madison, WI, USA) suite package [39]. A combination of several ω and φ scans with 0.5° rotation and 6 s per frame exposure time was used for the recording the half of the Ewald sphere ($\pm h, \pm k, \pm l$) up to $\theta_{\max} \sim 40^\circ$. Data reduction was performed using the following package: for the extraction of the reflection intensities and the correction of the Lorenz polarization effect was used the SAINT (Version 6.0, Bruker AXS Inc.: Madison, WI, USA) [40], for a semi-empirical absorption correction the SADABS (Version 2.10, University of Göttingen, Göttingen, Germany) [41] was adopted, and for the

calculation of the intensity statistics the XPREP (Version 2008/2, Bruker AXS Inc.: Madison, WI, USA) [42] was used. Least-squares refinement was performed using the program CRYSTALS (Version 12, University of Oxford, Oxford, UK) [43]. The refined parameters were scale factor, atom positions, anisotropic displacement parameters, and occupancies for extra framework anions. The relevant details of structure refinement are reported in Table S1 submitted as supplementary information. The CIF was deposited with the Cambridge Crystallographic Data Centre (CCDC 2,161,899). Figures showing structural details were prepared using the program VESTA (version 4.3.0, Tsukuba, Ibaraki, Japan) [44]. The distortion parameters were calculated according to [45] and [46]. Bond-valence sum (BVS) was calculated using the parameters by [47].

High-temperature X-ray powder diffraction (HTXRPD) data were collected in the air with a Bruker D8 ADVANCE powder diffractometer (Bruker AXS, Berlin, Germany) with Bragg–Brentano geometry (Cu-K α radiation, 40 kV, 40 mA), equipped with an HTK16 heating chamber. Stellerite grains were selected by hand picking at the binocular microscope and gently crushed by hand in an agate mortar. The stellerite powder, found to be single phase, was deposited on a PtRh substrate, assuring a direct homogeneous heating and fast temperature ramping.

Several experimental procedures have been elaborated to study the thermal behavior of the stellerite powder samples:

Experiment 1 (Exp. 1). Profiles were obtained between 6° and 60° 2 θ with a step size of 2 θ –0.02° and a counting time of 1 s per step. The temperature step of the heating and cooling rate was 10 °C/min stepwise at discrete steps of 50 °C up to 750 °C with an equilibration time of 1 min.

Experiment 2 (Exp. 2). Profiles were obtained between 6° and 45° 2 θ with a step size of 2 θ –0.02° and a counting time of 1 s per step. The temperature step of the heating and cooling rate was 10 °C/min stepwise at discrete steps of 10 °C up to 220 °C and down to 30 °C with an equilibration time of 1 min.

Experiment 3 (Exp. 3). Profiles were obtained between 6° and 45° 2 θ with a step size of 2 θ –0.02° and a counting time of 1 s per step. At first, the temperature was raised from room temperature to 200 °C at a rate of 10 °C/min. Then the temperature step of the heating and cooling rate was 10 °C/min stepwise at discrete steps of 10 °C up to 350 °C and down to 30 °C with an equilibration time of 1 min.

Experiment 4 (Exp. 4). Profiles were obtained between 6° and 45° 2 θ with a step size of 2 θ –0.02° and a counting time of 1 s per step. At first, the temperature was raised from room temperature to 350 °C at a rate of 10 °C/min. Then the temperature step of the heating and cooling rate was 10 °C/min stepwise at discrete steps of 10 °C up to 700 °C with an equilibration time of 1 min.

It took 32.5 min to record each diffraction pattern.

The TOPAS 4.2 software package (Bruker AXS, Berlin, Germany) [48] was used for Rietveld profile fitting and unit cell parameters calculation. The structural model of stellerite obtained by SCXRD was taken as a starting. The background was modeled using a Chebychev polynomial approximation of 8th order. The Rietveld refinement of the powder patterns converged successfully up to 120 °C. Above this temperature, the difficulty in the structure refinement and the appearance of new peaks suggested a phase transition. The stabilization of the patterns was evident above 140 °C, and the pattern at 150 °C was consistent with the structure of stellerite Phase B [12–16]. The peak profile was described by a pseudo-Voigt. Rietveld refinements were performed for all patterns and provided agreement factors, R_{wp} , in the range from 6.2 to 9.1%.

Heating to temperatures > 500 °C results in the collapse of the structure.

The coefficients of the thermal expansion tensor and the orientation of the principal axes of the thermal-expansion tensor with respect to the crystallographic axes were determined using the TEV program [49].

Infrared spectroscopy

Infrared (IR) absorption spectra of stellerite were obtained using an FTIR Simex FT-801 spectrophotometer (Simex, Novosibirsk, Russia). Powdered samples were mixed with anhydrous KBr, pelletized, and analyzed at a resolution of 2 cm^{-1} . A total of 32 scans were collected for each spectrum. The IR spectrum of an analogous pellet of pure KBr was used as a reference. FTIR reflection spectra were measured using a Simex Micran-3 FTIR microscope (Simex, Novosibirsk, Russia) equipped with an MCT detector with a resolution of 4 cm^{-1} . The aperture was $100 \times 100\ \mu\text{m}$, and a total of 32 scans were collected for each spectrum. The stainless mirror spectrum was used as a reference. Absorption spectra in the near-infrared (NIR) spectral region were registered using a Perkin-Elmer Lambda 950 spectrophotometer (Perkin-Elmer, Shelton, CT, USA).

The dehydration procedure was described in detail in [31–34, 50]. Powdered for FTIR and single-crystal samples for measuring the reflection and NIR absorption spectra were sequentially heated through 50 °C for an hour. After that, the transmission and reflection spectra were measured. At temperatures above 250 °C, single-crystal samples became brittle and were destroyed.

Results

Crystal chemistry

The studied crystals show intra-crystalline homogeneity and the chemical composition (see Table S2) results are very

close to those of the stellerite samples from Sardinia and Gibelsbach that have been previously analyzed by Galli (1973) [51], Alberti et al. (1978) [52] and Armbruster et al. (1996) [53].

The chemical formula of the investigated sample from Savinskoye is $\text{Ca}_{7.69}\text{Na}_{0.25}\text{K}_{0.06}(\text{Si}_{56.24}\text{Al}_{15.76})\text{O}_{144} \cdot 53.39\text{H}_2\text{O}$ (determined from six EPMA analyses on 5–8 analytical points, Table S2; water content was calculated assuming “Total wt%” = 100%).

The projection of the crystal structure along a -axis is shown in Fig. 1. The cell parameters, atomic coordinates and site occupancies, bond distances, and the main structural features of the single crystal investigated here are represented in Tables S1, S3, S4, and S5, respectively. The measured $\langle T\text{--O} \rangle$ distances range from 1.629 to 1.644 Å (Table S4) and it is possible to state that all the T positions have mixed occupancy (tetrahedral volume $\sim 2.22\text{--}2.28\ \text{Å}^3$; BVS $\sim 3.80\text{--}3.95$ valence units; Table S5). The reported formula evidences that in the analyzed crystals, the tetrahedral sites are occupied by Si and Al in a ratio $\text{Si}/(\text{Si} + \text{Al}) \sim 0.77$.

According to the crystal structure refinement, there are twelve water molecule positions (Ow8–Ow19, Table S3) in the zeolitic channels; the occupancies of Ow sites are 15–42%. The short distances between some of these positions ($1\text{--}2.5\ \text{Å}$) imply the statistical distribution of corresponding oxygen atoms. So, taking into account the average interatomic distance (Table S4; $\langle \text{Ca}\text{--Ow} \rangle \sim 2.427\ \text{Å}$; the calculated average valence force per Ca–Ow bond is 0.280 v.u.) and the sum of the valence forces of the Ca position (2 v.u.), we can conclude that a calcium atom can be simultaneously coordinated by no more than 7 oxygen atoms of water molecules.

HT XRPD

Selected XRPD patterns of stellerite are plotted in Fig. S3–S7 for Experiments 1–4. The unit cell parameters calculated at each step of heating and cooling are given in Tables S6–S9. Initial cell dimensions obtained from the powder data refinements are closed to those derived from SCXRD data (Table S1). In Fig. S8 and S9, the Rietveld refinement of the data obtained at 30 °C and 150 °C (Exp. 1) are shown. The evolution of the volume and unit cell parameters of stellerite as a function of temperature is plotted in Figs. 2, 3 and 4 and S10–S13.

The coefficients of the thermal expansion tensor and the orientation of the principal axes of the thermal-expansion tensor with respect to the crystallographic axes are listed in Tables S10–S17. A fourth- and third-order polynomial approximation of temperature dependencies has been used for experiments 1–4.

Since heating at temperatures > 500 °C results in the thermally induced collapse of the structure, we will discuss

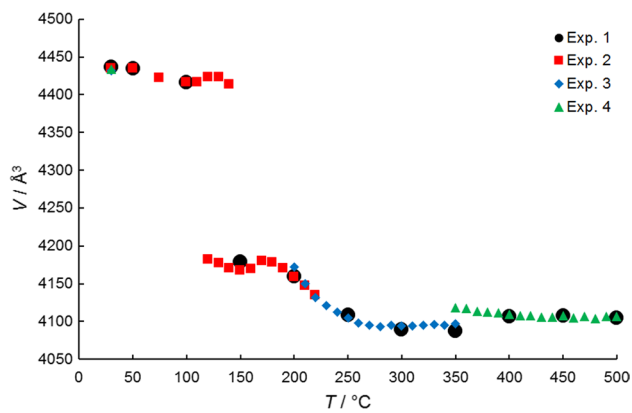


Fig. 2 Unit cell volume of stellerite vs temperature, obtained during Exp. 1 – black circles, Exp. 2 – red squares, Exp. 3 – blue diamonds and Exp. 4 – green triangles. Estimated standard deviations are smaller than the symbol used

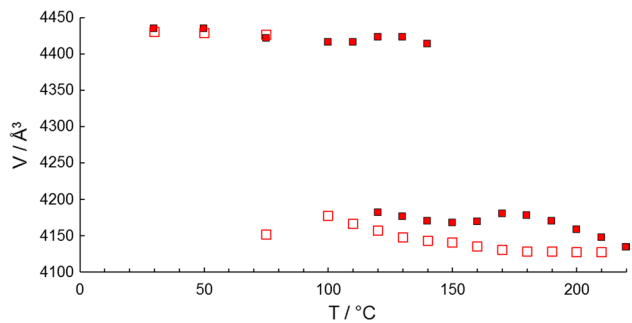


Fig. 3 Unit cell volume of stellerite vs temperature. Experiment 2. Symbols: solid for the heating, empty for the cooling. Estimated standard deviations are smaller than the symbol used

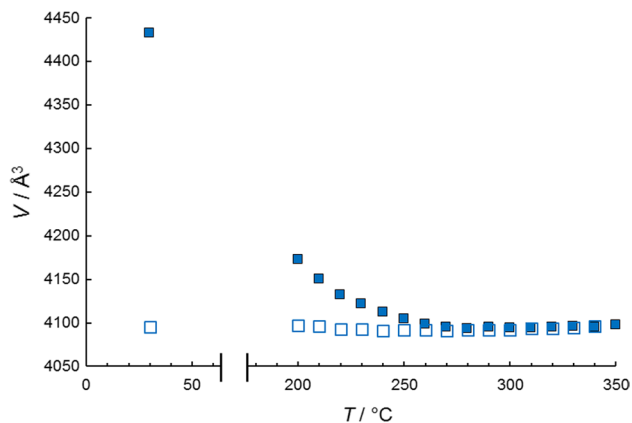


Fig. 4 Unit cell volume of stellerite vs temperature. Experiment 3. Symbols: solid for the heating, empty for the cooling. Estimated standard deviations are smaller than the symbol used

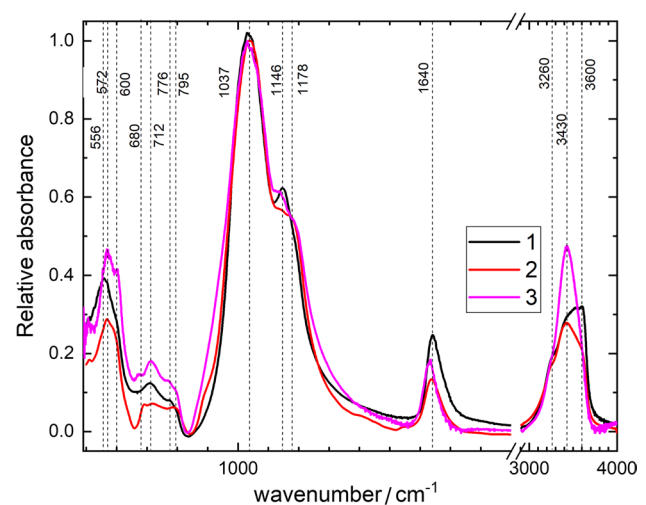


Fig. 5 Infrared absorption spectra of stellerite: 1 – before annealing; 2 – annealed at 200 °C and 3 – annealed at 400 °C for one hour

here the results obtained up to 500 °C from the diffraction patterns. Experiments carried out up to the indicated temperature include data on the cooling of stellerite samples.

IR spectroscopy

FTIR absorption spectra of initial and annealed powdered stellerite are given in Fig. 5. In the absorption spectrum of the stellerite before annealing (Fig. 5, curve 1) strong band at 1037 cm^{-1} , a strong shoulder at 1146 cm^{-1} were observed together with a band at 556 cm^{-1} , a weak band at 712 cm^{-1} and shoulder at 776 cm^{-1} . In addition, the bands at 1640 cm^{-1} and 3600 cm^{-1} with a shoulder at 3430 and 3260 cm^{-1} were found.

Change in the absorption spectra appears in the annealed samples (Fig. 5, curves 2 and 3). The band at 556 cm^{-1} is shifted to 572 cm^{-1} and shoulders at 600, 680, 795 cm^{-1} , and 1178 cm^{-1} were manifested. The intensity of the absorption bands at 1640 and 3430 cm^{-1} were decreased and the band at 3600 cm^{-1} disappeared. The difference between a single-crystal plate of stellerite, unheated and heated at a temperature of 200 °C, is clearly distinguishable in the IR reflection spectrum in the region of 1000–1500 cm^{-1} (Fig. S14).

Further heating slightly changed the spectra in the region of 490–3000 cm^{-1} (Fig. 5, curve 3). However, the intensity of the absorption band at 3430 cm^{-1} grew in the samples heated above 200 °C, while the intensity of the shoulder in the region of 3260 cm^{-1} on the contrary decreased.

Temperature dependence of integral intensities of the 3260, 3430, and 3600 cm^{-1} bands were given in Fig. 6. The intensity of the 3600 cm^{-1} band was strongly decreased at temperatures higher than 200 °C. The intensity of the 3430 cm^{-1} band is increased in the temperature interval of

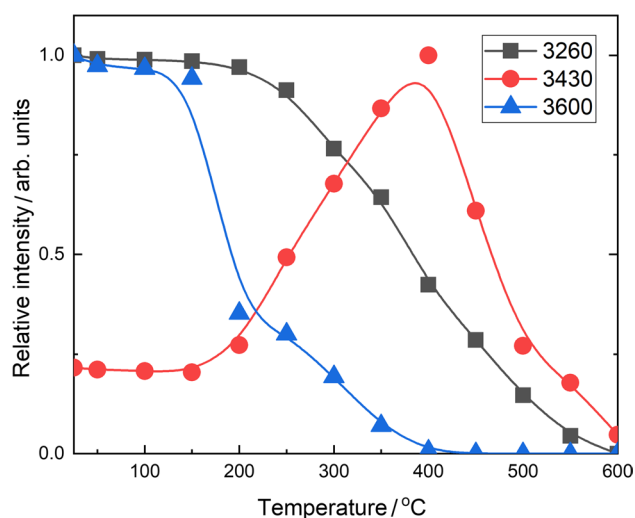


Fig. 6 Temperature dependences of integral intensities of absorption bands at 3260, 3430, and 3600 cm^{-1}

200–400 °C and then it falls. The intensity of the 3260 cm^{-1} band was decreased at a temperature higher than 250 °C.

In absorption spectra in the near-infrared region a doublet band at 7050 cm^{-1} and an intense band at 5240 cm^{-1} and shoulder at 5070 cm^{-1} were observed in the initial sample (Fig. 7). The heating for one hour at 150 °C involved to slightly decrease of 5240 cm^{-1} band. The bands at 7050 cm^{-1} are not changed. However, the intensity of the 5235 and 7050 cm^{-1} bands decreased after heating at 200 °C. At the same time, the band peaked at 4550 cm^{-1} appeared (the row in Fig. 7).

Discussion

HT XRPD

Annealing the sample leads to dehydration and to the fact that the structural framework loses the support of water molecules located in the channels. The Si-Al framework collapses with significant distortion, resulting in a subsequent decrease in symmetry. Arletti et al. (2006) [16] reported that it undergoes SBUs rotation, with subsequent zig-zag shaping of SBUs chains and statistical breaking of the TOT bridge in the four-membered ring.

To analyze our experimental results, we briefly summarize what previously reported in the literature (Table S18), since the conditions were somewhat different. Thus, Alberti et al. (1978) [13] refined the crystal structure of stellerite using SCXRD before and after heating the sample to a temperature of 220 °C. Arletti et al. (2006) [16] and Cametti et al. (2017) [17] performed in situ synchrotron XRPD and in situ SCXRD experiments, respectively. After annealing

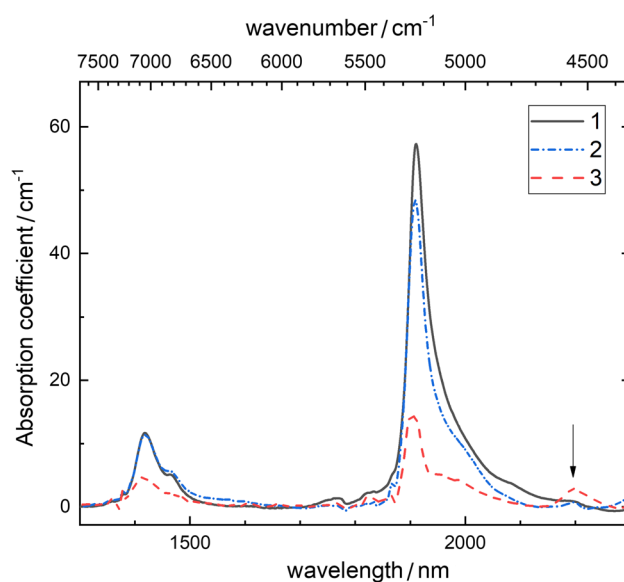


Fig. 7 Near-infrared absorption spectra of single-crystal stellerite plates before annealing (curve 1), annealed at 150 °C (curve 2) and 200 °C (curve 3) for one hour

and transition to the space group *Amma* (B-phase), the unit cell volume decreased by 12.4% [13], 7.8% [16], and 7.4% [17]. Arletti et al. (2006) [16] observed a smaller decrease in volume in the experiment with the powder with respect to the study of a single crystal [13] (8% versus 12% in) as well as Cametti et al. (2017) [17] had similar value to Arletti et al. (2006) [16], but it was obtained by an in situ single-crystal experiment. Different conditions—continuous and rapid heating in air and prolonged heating at constant temperature in a vacuum—can explain these discrepancies. So Arletti et al. (2006) [16] hypothesized that slower kinetics lead to a more collapsed and stable structure. In a powder experiment in the T range ~137–210 °C both A and B phases coexist [16]. Indeed, Alberti et al. (1978) [13] pointed out that the parameters of the unit cells measured under room conditions on powders preliminarily annealed at 200–400 °C are much larger than those obtained in the experiment with a single crystal. In contrast to other studies, at 300 °C Cametti et al. (2017) [17] refined the crystal structure of partially dehydrated stellerite in the monoclinic space group *A2/m* due to a strong disordering of distribution of Ca. According to Arletti et al. (2006) [16], after about a year in the air, rehydration occurs and the starting unit cell parameters of the natural phase are recovered.

However, in addition to heating the samples, we also paid attention to the kinetics of cooling.

Exp. 1. Figure 2 and S10 show the evolution of the volume and unit cell parameters of stellerite as a function of temperature. No modifications are observed in the diffraction patterns collected from 30 to 100 °C, being the peaks'

positions and intensities unchanged. In the temperature range between 100 and 150 °C, an A → B phase transition occurs ($Fm\bar{3}m \rightarrow Amma$). For $T > 150$ °C the pattern of Phase B only is observed.

A shrinkage along the [011] direction occurs at $T = 50\text{--}100$ °C (Table S14). The thermal expansivity coefficients are $\alpha a: \alpha b: \alpha c (\times 10^{-5}) = 2.50: -25.52: -6.84$ at 100 °C (Table S10). At 150 °C, after the completion of the phase transition, the compression proceeds along the [011] direction ($\alpha a: \alpha b: \alpha c (\times 10^{-5}) = 0.44: -21.75: -25.64$). At $T = 350\text{--}400$ °C the mineral exhibits a slight positive expansion for the [011] and [101] directions (Table S14) (the thermal expansivity coefficients are $\alpha a: \alpha b: \alpha c (\times 10^{-5}) = -0.80: 5.15: 8.46$ at 400 °C, Table S10). At the temperature of 500 °C stellerite shows a strong negative thermal expansion along the [001] direction (Table S14). The thermal expansivity coefficients are $\alpha a: \alpha b: \alpha c (\times 10^{-5}) = 3.06: -1.86: -16.94$ at 500 °C (Table S10).

It is noted that the parameters of the unit cell after heating changed unevenly. Therefore, parameters b and c decreased by 3.9 and 3.8%, respectively, while the change for the parameter a is 0.02%. The unit cell volume decreased by 7.5%.

Exp. 2. The only phase present between room temperature and 110 °C is stellerite Phase A (space group $Fm\bar{3}m$) and the unit cell parameter variations in this T range are 0.07, -0.33, and -0.17%, for a , b , and c , respectively, with a volume contraction of 0.42% (Table S7). In the temperature range of 120–140 °C, a phase transition to Phase B (space group $Amma$) occurs and both A and B Phases coexist (Fig. 3, S11). The volume further contracts by about 0.22% for the A Phase and 0.28% for the B Phase. Above 150 °C only stellerite Phase B is stable. In the temperature range of 150–220 °C, stabilization of the cell parameters is observed and the total decrease in unit cell volume at 220 °C is about 6.8%.

The graphical representation of the thermal expansion of the stellerite in the T range of 50–220 °C is displayed in Table S15. At $T = 50\text{--}110$ °C the mineral exhibits a negative expansion in all directions. In the temperature range of 120–140 °C, a phase transition occurs, while at $T = 150$ °C the thermal expansivity coefficients are similar to that at 110 °C (Table S11). Negative axial expansion for Phase B in the temperature range of 150–190 °C is anisotropic, with $\alpha a: \alpha b: \alpha c (\times 10^{-5})$ are 4.88: -43.23: -33.57 at 150 °C and -2.55: -1.52: -18.75 at 190 °C. A positive expansion along the b direction occurs at $T = 200$ °C (Table S15).

Compared to Exp. 1, where a positive thermal expansion appears in the temperature range 250–300 °C, in Exp. 2 (which is slower and longer), the expansion is fixed at lower temperatures.

The values of the unit cell parameters refined at room temperature after the cooling of the sample are not the same

obtained before the direct experiment (see Table S11). At the same time, the volume of the unit cell remained the same (Fig. 3). The reverse transition of Phase B to Phase A occurs at temperatures below 100 °C (Fig. 3). At 75 °C these two phases coexist, but at 50 °C the phase transition is complete.

After stepwise cooling the stellerite sample (from 220 to 30 °C), the unit cell volume increased by 7.2%, but the decrease was 0.1% relative to the initial value before heating (Table S7).

Exp. 3. In this experiment, the stellerite was relatively quickly heated from 30 to 200 °C; the heating time was 17 min. The diffraction patterns obtained in the temperature range of 280–350 °C were examined more carefully, taking into account the expectation of the appearance of a highly disordered stellerite phase having a different space group [17]. No evidences for the appearance of this Phase D in the patterns were found. However, we note that further HT SCXRD studies are needed to confirm this statement. At the temperature point of 350 °C, the unit cell volume value decreases by 7.6% (Fig. 4, Table S8).

An examination of the coefficients of the thermal expansion tensor and the orientation of the principal axes of the thermal-expansion tensor with respect to the crystallographic axes indicates that during Exp. 3, completion of the negative thermal expansion process and the start of the positive one along the [100] direction is shifted towards lower temperatures with respect to the results of Exp. 1. Compression along the abovementioned direction ends at 310 °C (Table S16). The expansion along [100] starts at 320 °C, while in Exp. 1, such expansion begins only in the range of 350–400 °C. The thermal expansivity coefficients are $\alpha a: \alpha b: \alpha c (\times 10^{-5}) = -0.41: -0.18: -2.31$ at 300 °C and 1.84: -0.91: 3.16 at 320 °C (Table S12).

No evidence of Phase B → Phase A transition was observed within the cooling T range investigated and all the diffraction patterns (350–30 °C) were successfully indexed in the $Amma$ space group. The unit cell volume variation as a function of T is shown in Fig. S12. The measured evolution of the unit cell parameters is shown in Fig. 4. After rapid cooling (from 200 to 30 °C, 17 min), there was no significant change in the value of the cell volume (Table S8).

Exp. 4. Unit cell parameters values refined at each step of heating are plotted in Fig. S13 and Table S9. Axial expansion for stellerite rapidly preheated to 350 °C (the time taken to raise the temperature was 32 min) is anisotropic. In this case, the values of the thermal expansivity coefficients (Tables S13 and S17) change very smoothly, which indicates the smoothness of the ongoing kinetic processes. The thermal expansivity coefficients are $\alpha a: \alpha b: \alpha c (\times 10^{-5}) = 0.76: -2.12: -1.61$ at 400 °C and 2.22: -2.51: 1.09 at 500 °C (Table S13). Relative to Experiment 1, the temperatures of the onset of positive expansion are shifted towards higher values. The positive expansion along the [101]

direction starts at 420 °C, gradually changing its direction to the [100].

No evidence of phase transition and occurrence of new diffraction peaks in the powder patterns were observed above 300 °C, suggesting the absence of a further phase transition to a new phase, highly deformed stellerite D ([17], Table S18). In general, the volume of the unit cell when heated to 500 °C decreased by 7.4%, while the parameter a increased by 0.5%, and the b and c decreased by 4% (Table S9, Fig. S13).

Finally, paying attention to Fig. 2, it can be noted that the reduction in the unit cell volume occurs more slowly with faster heating. So, it is obvious that at 200 °C the V value in Exp. 3 is 0.3% larger than that in Exp. 1 and at 350 °C the V value in Exp. 4 is 0.5% larger than that in Exp. 1.

As a result, the important thing to note is that the slower we carried out the heating, the faster the thermal expansivity processes proceeded.

Analyzing the trend of the thermal behavior of the crystal structure of stellerite, which is common for all four experiments, we note that relatively isotropic compression and expansion are typical in the direction perpendicular to the a axis. The aluminosilicate chains, extended along the c axis, connecting with neighboring chains, form large cavities. These cavities have wide apertures along the a axis. When water molecules leave these structural pores, the cavities naturally narrow in directions perpendicular to the channels (along the b and c axes). Further thermal expansion has a similar character.

IR spectroscopy

The band at 556 cm^{-1} in the untreated and at 572 cm^{-1} in the heated stellerite are attributed to the 4-membered ring breathing modes [54]. The asymmetric stretching modes of the TO_4 ($T=\text{Si}$ and Al) framework are around 1037 cm^{-1} with a shoulder extending to 1146 cm^{-1} . The symmetric stretching T–O vibration AlO–H deformation modes are located in the region 670–800 cm^{-1} [28]. The O–H modes are also involved in the framework vibrations [31, 53]. The band at 1640 cm^{-1} is attributed to bending vibrations of zeolite water molecules. The band at 3600 cm^{-1} and the shoulders at 3260 cm^{-1} and 3430 cm^{-1} correspond to the stretching vibration of zeolite water [55, 56]. In a heated above 200 °C sample the band at 3600 cm^{-1} disappears due to phase transitions. The further heating leads to an increase of 3430 cm^{-1} band and a decrease of 3260 cm^{-1} band. That is the evidence that H_2O molecules concentrate in specific positions in zeolite cages. The heating above 400 °C causes complete dehydration of the stellerite. The intensity of 3430 cm^{-1} and 3260 cm^{-1} bands are decreased that is accompanied by the decrease of unit cell volume. Thus, at about 260 °C, the initial eleven water molecules are distributed

over two positions [16]. Above this temperature, the water content steadily decreases, and at about 360 °C H_2O is concentrated in only one structural position [16].

The most changes in the far-IR active modes are the shift of the 4-membered ring breathing vibrational modes in the heated samples. The frequency increase is about 16 cm^{-1} compared to unheated stellerite (Fig. 5, curves 2 and 3). This is consistent with our X-ray diffraction refinement results where, however, the phase transition takes place at lower temperatures (about 150 °C). A similar blue shift of 4-membered ring mode was found in cation-exchanged stilbite. These modes are also found to be sensitive to the changes in the chain rotation angle and could be used as an indicator of H_2O molecules' arrangement in stilbites [57].

The phase transition is also detected in FTIR reflectance spectra, where the band attributed to the asymmetric stretching vibration of T–O is shifted by 35 cm^{-1} (Fig. S14). This is due to changes in chain rotation angle and arrangement of H_2O molecules that participated in the framework vibrations [53, 58].

The near-infrared absorption spectrum of stellerite is also sufficiently changed after heating above 200 °C (Fig. 7). The observed bands at 5070, 5240, and 7050 cm^{-1} correspond to overtones of water molecules and hydroxyl vibration. The band at 5070 cm^{-1} is a combination of the libration and stretching modes. The band at 5240 cm^{-1} is a combination of the stretching modes of H_2O and the 7050 cm^{-1} band is an overtone of OH^- stretching vibrations [59]. These bands decrease after the heating, but the band at 4550 cm^{-1} appears. A similar behavior during heating was observed in stilbite [30] and heulandite [60, 61] at the temperatures of phase transition A \rightarrow B. The increase of the 4550 cm^{-1} band intensity could be the evidence of zeolitic water arrangement after Phase A \rightarrow Phase B transition.

Conclusion

Knowledge of the thermal behavior of zeolites may allow us to obtain useful information for possible technological applications. This investigation and the papers devoted to the study of the minerals of the stilbite group, in particular stellerite [13, 16, 17], give a clear idea that the manifestation of thermal characteristics is strongly influenced by heating conditions.

It is noted that in continuous experiments, for example, in situ SCXRD study by Cametti et al. (2017) [17], we may see a slow development of the unit cell volumes with temperature and gradual transitions from A to B phases of stellerite. On the contrary, in fast studies, for example, in situ synchrotron XRPD by Arletti et al. (2006) [16], the A \rightarrow B transition is shifted towards higher temperatures and is rather abrupt. Cametti et al. (2017) [17] also concluded that

the main difference in the modification of the stellerite B phase between their results and those of Alberti et al. (1978) [13] is most likely not due to the difference in methods—in situ and ex situ—but due to a different heating and dehydration procedure. The details of the differences in the crystal structures of stellerite heated under different conditions could be found in [17].

In our in situ HTXRPD experiments, it is noted that, depending on the heating rate of the sample, the model of temperature behavior changes, although not very significantly. The most important difference is the temperature barriers for the beginning and end of the processes of thermal expansion and contraction in different directions of the crystal structure of the sample under study.

An important part of this work is the conclusion that the dynamics of the structural changes of stellerite with increasing temperature can be traced using Infrared spectroscopy and microscopy.

An additional noteworthy point emerging from this study is that there is a significant difference between the results obtained with in situ X-ray powder diffraction and ex situ powder IR spectroscopy. Our results confirm the conclusion about the dependence of the phase transition temperature on the experimental components (heating rate and duration of the experiment). According to the FTIR data, the Phase A → Phase B transition of stellerite occurs at higher temperatures than during the HTXRPD experiment. The reversibility/irreversibility of the A → B transition as a function of maximum T achieved is dependent on kinetics of cooling and should be studied in more detail.

Supplementary Information The online version contains supplementary material available at <https://doi.org/10.1007/s44211-022-00186-4>.

Acknowledgements This research was supported by the governmental assignment in terms of Project 0284-2021-0005. The stellerite specimens studied in this work were kindly provided by the staff of Sidorov Mineralogical Museum of INRTU. The study was carried out using the facilities of the Centers for Collective Use: “Center for isotopic-geochemical investigations” at the Vinogradov Institute of Geochemistry SB RAS and “Baikal analytical center for collective use” at the Favorsky Irkutsk Institute of Chemistry SB RAS. We are grateful to reviewers for their valuable comments.

Author contributions The manuscript was written through contributions of all authors. All authors have given approval to the final version of the manuscript.

Data availability All data generated or analysed during this study are included in this published article (and its supplementary information files).

Declarations

Conflict of interest The authors declare that there are no conflicts to declare.

References

1. C. Baerlocher, L.B. McCusker, D.H. Olson, *Atlas of zeolite framework type* (Elsevier BV, Amsterdam, 2007). <https://doi.org/10.1016/B978-0-444-53064-6.X5186-X>
2. W.O. Milligan, H.B. Weiser, *J. Phys. Chem.* **41**, 1029 (1937)
3. M. Koizumi, R. Kiriyama, *Sci. Rept. (Osaka Univ.)* **2**, 67 (1953)
4. E. Pécsi-Donàth, *Acta Acad. Sci. Hung.* **9**, 235 (1965)
5. F. Aumento, *Can. J. Earth Sci.* **3**, 351 (1966)
6. M.S. Joshi, P.M. Rao, A.L. Choudhari, R.G. Kanitkar, *Thermochim. Acta.* **58**, 79 (1982)
7. E. Galli, A. Alberti, *Bull. Soc. Fr. Minéral. Cristallogr.* **98**, 331 (1975). <https://doi.org/10.3406/bulmi.1975.7013>
8. M. Sacerdoti, A. Sani, G. Vezzalini, *Micr. Mes. Mater.* **30**, 103 (1999). [https://doi.org/10.1016/S1387-1811\(99\)00028-1](https://doi.org/10.1016/S1387-1811(99)00028-1)
9. M. Slaughter, *Amer. Min.* **55**(3–4), 387 (1970)
10. E. Galli, *Acta Cryst.* **B27**, 833 (1971). <https://doi.org/10.1107/S056774087100298X>
11. G. Cruciani, G. Artioli, A. Gualtieri, K. Ståhl, J. Hanson, *Amer. Min.* **82**, 729 (1997). <https://doi.org/10.2138/am-1997-7-810>
12. E. Galli, A. Alberti, *Bull. Soc. Fr. Minéral. Cristallogr.* **98**, 11 (1975). <https://doi.org/10.3406/bulmi.1975.6952>
13. A. Alberti, R. Rinaldi, G. Vezzalini, *Phys. Chem. Minerals.* **2**, 365 (1978)
14. S.A. Miller, J.C. Taylor, *Zeolites* **5**, 7 (1985). [https://doi.org/10.1016/0144-2449\(85\)90003-X](https://doi.org/10.1016/0144-2449(85)90003-X)
15. F. Pechar, G. Mattern, *Cryst. Res. Technol.* **21**(8), 1029 (1986)
16. R. Arletti, E. Mazzucato, G. Vezzalini, *Amer. Min.* **91**, 628 (2006). <https://doi.org/10.2138/am.2006.1966>
17. G. Cametti, M. Fisch, T. Armbruster, *Micr. Mes. Mat.* **253**, 239 (2017). <https://doi.org/10.1016/j.micromeso.2017.06.051>
18. S. Ori, E. Mazzucato, G. Vezzalini, *Amer. Min.* **94**, 64 (2009). <https://doi.org/10.2138/am.2009.2914>
19. V.A. Drebuschak, S.N. Dementiev, Yu.V. Seryotkin, *J. Therm. Anal. Calorim.* **107**, 1293 (2012). <https://doi.org/10.1007/s10973-011-1608-4>
20. M. Sacerdoti, *Micr. Mes. Mat.* **102**, 299 (2007). <https://doi.org/10.1016/j.micromeso.2007.01.012>
21. G. Cametti, T. Armbruster, M. Nagashima, *Micr. Mes. Mat.* **236**, 71 (2016). <https://doi.org/10.1016/j.micromeso.2016.08.023>
22. A. Alberti, A. Martucci, *Stud. Surf. Sci. Catal.* **155**, 19 (2005). [https://doi.org/10.1016/S0167-2991\(05\)80135-1](https://doi.org/10.1016/S0167-2991(05)80135-1)
23. G. Cametti, A.C. Scheinost, M. Giordani, S.V. Churakov, *J. Phys. Chem. C.* **23**, 13651 (2019). <https://doi.org/10.1021/acs.jpcc.9b01976>
24. G. Cametti, A.C. Scheinost, S.V. Churakov, *J. Phys. Chem. C.* **123**, 25236 (2019). <https://doi.org/10.1021/acs.jpcc.9b07297>
25. Yu.V. Seryotkin, V.V. Bakakin, AYu. Likhacheva, S.V. Rashchenko, *J. Struct. Chem.* **53**, 26 (2012). <https://doi.org/10.1134/S0022476612070049>
26. Yu.V. Seryotkin, V.V. Bakakin, *J. Struct. Chem.* **60**(10), 1612 (2016). <https://doi.org/10.1134/S0022476619100068>
27. Yu.V. Seryotkin, S.N. Dementiev, AYu. Likhacheva, *Phys. Chem. Min.* **48**, 4 (2021). <https://doi.org/10.1007/s00269-020-01131-5>
28. F. Pechar, D. Rykl, *Chem. Pap.* **35**(2), 189 (1981)
29. X. Zhang, C. Zhang, F. Zhan, N. Chen, *Key Eng. Mater.* **591**, 12 (2014). <https://doi.org/10.4028/www.scientific.net/KEM.591.12>
30. P.S.R. Prasad, K. Shiva Prasad, S. Ramana Murthy, *Amer. Min.* **90**, 1636 (2005)
31. E. Kaneva, A. Bogdanov, R. Shendrik, *Structural and vibrational properties of agrellite*. *Sci. Rep.* **10**, 15569 (2020). <https://doi.org/10.1038/s41598-020-72631-1>
32. E.V. Kaneva, T.A. Radomskaya, R.Yu. Shendrik, V.M. Chubarov, A.A. Amosova, M.A. Mitichkin, 2020 in *Minerals: Structure, Properties, Methods of Investigation*, eds. by S. Votyakov, D.

- Kiseleva, V. Grokhovskiy, Y. Shchapova (Springer Proceedings in Earth and Environmental Sciences. Springer, Cham.), p. 97.
33. E. Kaneva, T. Radomskaya, R. Shendrik, V. Chubarov, V. Danilovskiy, *Minerals* **11**, 1049 (2021). <https://doi.org/10.3390/min11101049>
 34. E. Kaneva, R. Shendrik, *Curr. Comput.-Aided Drug Des.* **12**, 377 (2022). <https://doi.org/10.3390/cryst12030377>
 35. G.M. Lobanova, B.P. Sanin, *Trudy IGEM AN SSSR* **83**, 147 (1963)
 36. K.S. Taldykina, *Mineralogy of polymetallic deposits of the Klichka group of Eastern Transbaikalia*, Eds. AN SSSR, Moscow Leningrad (1962).
 37. K.S. Taldykina, *Proc. Russ. Mineral. Soc.* **87**(1), 106 (1958)
 38. I.L. Pouchou, F. Pichoir, PaP (phi-rho-z) procedure for improved quantitative microanalysis. in *Microbeam analysis*, ed. by I.T. Armstrong (San Francisco Press, San Francisco, USA, 1985) pp. 104–106
 39. A.X.S.A.P.E.X. Bruker, *Version 201411-0* (Madison WI, USA, 2014)
 40. A.X. Bruker, *SAINT, version 6.0* (Bruker AXS Inc., Madison, WI, USA, 2007)
 41. G.M. Sheldrick, *SADABS, Program for Empirical Absorption Correction of Area Detector Data* (University of Göttingen, Göttingen, Germany, 2003)
 42. G.M. Sheldrick, *XPREP, version 2008/2* (Bruker AXS Inc., Madison, WI, USA, 2008)
 43. P.W. Betteridge, J.R. Carruthers, R.I. Cooper, K. Prout, D.J. Watkin, *J. App. Cryst.* **36**, 1487 (2003). <https://doi.org/10.1107/S0021889803021800>
 44. K. Momma, F. Izumi, *J. Appl. Crystallogr.* **44**, 1272 (2011). <https://doi.org/10.1107/S0021889811038970>
 45. K. Robinson, G.V. Gibbs, P.H. Ribbe, *Science* **172**, 567 (1971). <https://doi.org/10.1126/science.172.3983.567>
 46. B. Renner, G. Lehmann, *Z. Kristallogr.* **175**, 43 (1986). <https://doi.org/10.1524/zkri.1986.175.14.43>
 47. O.C. Gagnè, F.C. Hawthorne, *Acta Cryst.* **B71**, 562 (2015). <https://doi.org/10.1107/S2052520615016297>
 48. A.X.S. Bruker, *Topas V4. General Profile and Structure Analysis Software for Powder Diffraction Data* (Bruker AXS Inc., Karlsruhe, 2008)
 49. T. Langreiter, V. Kahlenberg, *Curr. Comput.-Aided Drug Des.* **5**, 143 (2015). <https://doi.org/10.3390/cryst5010143>
 50. A.N. Sapozhnikov, V.L. Tauson, S.V. Lipko, R.Y. Shendrik, V.I. Levitskii, L.F. Suvorova, N.V. Chukanov, M.F. Vigasina, *Amer. Min.* **106**(2), 226 (2021). <https://doi.org/10.2138/am-2020-7317>
 51. E. Galli, E. Passaglia, *Lithos* **6**, 83 (1973). [https://doi.org/10.1016/0024-4937\(73\)90081-9](https://doi.org/10.1016/0024-4937(73)90081-9)
 52. Th. Armbruster, Th. Kohler, Th. Meisel, Th.F. Nägler, M.A. Götzinger, H.A. Stalder, *Schweiz. Mineral. Petrogr. Mitt.* **76**, 131 (1996). <https://doi.org/10.5169/seals-57692>
 53. A. Bogdanov, E. Kaneva, R. Shendrik, *Materials* **14**(9), 2160 (2021). <https://doi.org/10.3390/ma14092160>
 54. T. Uchino, Y. Tokuda, T. Yokoi, *Phys. Rev. B* **58**(9), 5322 (1998). <https://doi.org/10.1103/PhysRevB.58.5322>
 55. M. Alkan, Ç. Hopa, Z. Yilmaz, H. Güler, *Micr. Mes. Mat.* **86**(1–3), 176 (2005). <https://doi.org/10.1016/j.micromeso.2005.07.008>
 56. X. Zang, S.P. Sander, *J. Phys. Chem. A* **115**(35), 9854 (2011). <https://doi.org/10.1021/jp203739v>
 57. Y. Ma, Z. Liu, A. Geng, T. Vogt, Y. Lee, *Micr. Mes. Mat.* **224**, 339 (2016). <https://doi.org/10.1016/j.micromeso.2016.01.005>
 58. J. Singh, R.L. White, *Spectrochim. Acta A Mol. Biomol. Spectrosc.* **231**, 118142 (2020). <https://doi.org/10.1016/j.saa.2020.118142>
 59. R.L. Frost, O.B. Locos, H. Ruan, J.T. Klopogge, *Vib. Spectrosc.* **27**(1), 1 (2001). [https://doi.org/10.1016/S0924-2031\(01\)00110-2](https://doi.org/10.1016/S0924-2031(01)00110-2)
 60. A. Alberti, G. Vezzalini, F. Cariati, L. Erre, P. Piu, *Zeolites* **5**(5), 289 (1985). [https://doi.org/10.1016/0144-2449\(85\)90160-5](https://doi.org/10.1016/0144-2449(85)90160-5)
 61. A. Alberti, G. Vezzalini, S. Quartieri, G. Cruciani, S. Bordiga, *Micr. Mes. Mat.* **42**(2–3), 277 (2001). [https://doi.org/10.1016/S1387-1811\(00\)00330-9](https://doi.org/10.1016/S1387-1811(00)00330-9)

Springer Nature or its licensor holds exclusive rights to this article under a publishing agreement with the author(s) or other rightsholder(s); author self-archiving of the accepted manuscript version of this article is solely governed by the terms of such publishing agreement and applicable law.